Quantifying the impact of aerosol scattering on the retrieval of methane from airborne remote sensing measurements

Yunxia Huang[1,2], Vijay Natraj[3], Zhaocheng Zeng[2,4], Pushkar Kopparla[5], and Yuk L. Yung[2,3]

[1]School of Science, Nantong University, Nantong, 226007, China

[2]Division of Geological and Planetary Sciences, California Institute of Technology, Pasadena, CA 91125, USA

[3]Jet Propulsion Laboratory, California Institute of Technology, Pasadena, CA 91109, USA

[4]Joint Institute for Regional Earth System Science and Engineering, University of California, Los Angeles, CA 90095, USA

[5]Graduate School of Frontier Sciences, The University of Tokyo, Kashiwa, Chiba 277-0882, Japan

Correspondence to: Vijay Natraj (vijay.natraj@jpl.nasa.gov)

Abstract. As a greenhouse gas with strong global warming potential, atmospheric methane (CH_4) emissions have attracted a great deal of attention. Although remote sensing measurements can provide information about CH_4 sources and emissions, accurate retrieval is challenging due to the influence of atmospheric aerosol scattering. In this study, imaging spectroscopic measurements from the Airborne Visible/Infrared Imaging Spectrometer–Next Generation (AVIRIS-NG) in the short-wave infrared are used to compare two retrieval techniques — the traditional Matched Filter (MF) method and the Optimal Estimation (OE) method, which is a popular approach for trace gas retrievals. Using a numerically efficient two-stream-exact-single-scattering radiative transfer model, we also simulate AVIRIS-NG measurements for different scenarios and quantify the impact of aerosol scattering in the two retrieval schemes by including aerosols in the simulations but not in the retrievals. The presence of aerosols causes an underestimation of CH_4 in both the MF and OE retrievals; the biases increase with increasing surface albedo and aerosol optical depth (AOD). Aerosol types with high single scattering albedo and low asymmetry parameter (such as water soluble aerosols) induce large biases in the retrieval. When scattering effects are neglected, the MF method exhibits lower fractional retrieval bias compared to the OE method at high CH_4 concentrations (2–5 times typical background values), and is suitable for detecting strong CH_4 emissions. For an AOD value of 0.3, the fractional biases of the MF retrievals are

between 1.3 and 4.5%, while the corresponding values for OE retrievals are in the 2.8–5.6% range. On the other hand, the OE method is an optimal technique for diffuse sources (<1.5 times typical background values), showing up to five times smaller fractional retrieval bias (8.6%) than the MF method (42.6%) for the same AOD scenario. However, when aerosol scattering is significant, the OE method is superior since it provides a means to reduce biases by simultaneously retrieving AOD, surface albedo and CH_4. The results indicate that, while the MF method is good for plume detection, the OE method should be employed to quantify CH_4 concentrations, especially in the presence of aerosol scattering.

1 Introduction

Atmospheric methane (CH_4) is about 85 times more potent per unit mass at warming the Earth than carbon dioxide (CO_2) on a 20-year timescale (IPCC, 2013), implying that reduction in CH_4 emissions could be very efficient to slow down global warming in the near term. Global mean CH_4 concentrations have increased from ~700 ppb in the preindustrial era to more than 1860 ppb as of 2019 (NOAA, 2019). The most effective sink of atmospheric CH_4 is the hydroxyl radical (OH) in the troposphere. CH_4 reacts with OH to reduce the oxidizing capacity of the atmosphere and generate tropospheric ozone. Increasing emissions of CH_4 reduce the concentration of OH in the atmosphere. With less OH to react with, the lifespan of CH_4 could also increase, resulting in greater CH_4 concentrations (Holmes et al., 2013). Soils also act as a major sink for atmospheric methane through the methanotrophic bacteria that reside within them.

Significant natural CH_4 sources include wetlands (Bubier et al., 1994, Macdonald et al., 1998; Gedney et al., 2004), geological seeps (Kvenvolden and Rogers, 2005; Etiope et al., 2009), ruminant animals, and termites. In addition, increased surface and ocean temperatures associated with global warming may increase CH_4 emissions from melting permafrost (Woodwell et al., 1998; Walter et al., 2006; Schaefer et al., 2014, Schuur et al., 2015) and methane hydrate destabilization (Kvenvolden, 1988; Archer, 2007). Human activity also contributes significantly to the total CH_4 emissions. Rice agriculture is one of the most important anthropogenic sources of CH_4 (Herrero et al., 2016; Schaefer et al., 2016). Other sources include landfills (Themelis and Ulloa, 2007), wastewater treatment, biomass burning, and methane slip from gas engines. Global fugitive CH_4 emissions from coal mining (Kort et al., 2014), natural gas and oil systems (Alvarez et al., 2018), hydraulic fracturing ("fracking") of shale gas wells (Howarth et al., 2011; Howarth, 2015, 2019), and residential and commercial natural gas distribution sectors (He et al., 2019) are also of increasing concern. Although the sources and sinks of methane are reasonably well known, there are large uncertainties in their relative amounts and in the partitioning between natural and anthropogenic contributions (Nisbet et al., 2014, 2016). This uncertainty is exemplified by the CH_4 "hiatus", which refers to the observed stabilization of atmospheric CH_4 concentrations from 1999–2006, and the renewed rise thereafter (Kirschke et al., 2013).

Satellite monitoring of CH_4 can be broadly divided into three categories: solar backscatter, thermal emission and lidar (Jacob et al., 2016). The first solar backscattering mission was SCIAMACHY (Frankenberg et al., 2006), which was operational from 2003–2012 and observed the entire planet once every seven days. It was followed by GOSAT in 2009 (Kuze et al., 2016), and subsequently the next generation GOSAT-2 in 2018 (Glumb et al., 2014). In between, the TROPOMI mission was also launched in 2017, which observes the planet once daily with a high spatial resolution of 7×7 km^2 (Butz

et al., 2012; Veefkind et al., 2012). CarbonSat (Buchwitz et al., 2013) is another proposed mission to measure CH_4 globally from solar backscatter with a very fine spatial resolution (2×2 km^2) and high precision (0.4%). GHGSat-D (McKeever et al., 2017; Varon et al., 2019; Jervis et al., 2020) measures between 1630–1675 nm, with an effective pixel resolution of 50×50 m^2 over targeted 12×12 km^2 scenes, and is intended to detect CH_4 emissions from individual industrial sites. In contrast, MethaneSAT (Wofsy and Hamburg, 2019) has a pixel size of 1–2 km^2 and a wide field of view (200 km^2) and can quantify diffuse CH_4 emission sources over large areas. Thermal infrared observations of CH_4 are available from the IMG (Clerbaux et al., 2003), AIRS (Xiong et al., 2008), TES (Worden et al., 2012), IASI (Xiong et al., 2013), and CrIS (Gambacorta et al., 2016) instruments. These instruments provide day/night measurements at spatial resolutions ranging from 5×8 km^2 (TES) to 45×45 km^2 (AIRS). GEO-CAPE (Fishman et al., 2012), GeoFTS (Xi et al., 2015), G3E (Butz et al., 2015), and GeoCarb (Polonsky et al., 2014) are proposed geostationary instruments (GeoCarb was selected by NASA under the Earth Venture - Mission program), which when operational will have resolutions of 2–5 km over regional scales. The MERLIN lidar instrument (Kiemle et al., 2014) scheduled for launch in 2021 will measure CH_4 by employing a differential absorption lidar.

By combining a large number of footprints and high spatial resolution, airborne imaging spectrometers are also well suited for mapping local CH_4 plumes. The Airborne Visible/Infrared Imaging Spectrometer–Next Generation (AVIRIS-NG) measures reflected solar radiance across more than 400 channels between 380 and 2500 nm (Green et al., 1998; Thompson et al., 2015). Strong CH_4 absorption features present between 2100 and 2500 nm can be observed at a spectral resolution of 5 nm full width at half maximum (FWHM). A number of approaches have been developed to retrieve CH_4 from such hyperspectral data. Roberts et al. (2010) used a spectral residual approach between 2000 and 2500 nm and Bradley et al. (2011) employed a band ratio technique using the 2298 nm CH_4 absorption band and 2058 nm CO_2 absorption band. However, these techniques are not suited for terrestrial locations that have lower albedos and have spectral structure in the SWIR. A cluster-tuned matched filter technique was demonstrated to be capable of mapping CH_4 plumes from marine and terrestrial sources (Thorpe et al., 2013) as well as CO_2 from power plants (Dennison et al., 2013); however, this method does not directly quantify gas concentrations. Frankenberg et al. (2005) developed an iterative maximum *a posteriori* differential optical absorption spectroscopy (IMAP-DOAS) algorithm that allows for uncertainty estimation. Thorpe et al. (2014) adapted the IMAP-DOAS algorithm for gas detection in AVIRIS imagery. In addition, they developed a hybrid approach using singular value decomposition and IMAP-DOAS as a complementary method of quantifying gas concentrations within complex AVIRIS scenes.

Accurate assessment of CH_4 emissions is particularly challenging in the presence of aerosols because the latter introduce uncertainties in the light path if not accounted for. In fact, CH_4 emissions are frequently correlated with pollution due to concurrent aerosol emissions. For large aerosols (such as dust), the low Ångström exponent values result in high aerosol optical depth (AOD) values even in the wavelength range from 2000 nm to 2500 nm (Seinfeld and Pandis, 2006; Zhang et al., 2015). Therefore, it is important to obtain a clear understanding of aerosol impacts on CH_4 retrievals. In this study, SWIR AVIRIS-NG measurements are used to analyze the impact of aerosol scattering on CH_4 retrievals. Further, using an accurate but numerically efficient radiative transfer (RT) model (Spurr and Natraj, 2011), we simulate AVIRIS-NG measurements with varying aerosol amounts and quantify the impact of aerosol scattering using two retrieval techniques, the traditional matched filter (MF) method and the optimal estimation (OE) method that is widely used in trace gas remote sensing. This article is organized as follows. The MF and OE retrieval methods are described in Section 2. Section 3 focuses on analysis of a sample CH_4 plume detected by AVIRIS-NG measurements and compares retrievals using the MF and OE methods. Section 4 presents a detailed evaluation of aerosol impacts on the two retrieval methods through simulations of AVIRIS-NG spectra for different geophysical parameters. Section 5 provides a summary of the work and discusses future research.

2 Methods

2.1 MF method

Real-time remote detection using AVIRIS-NG measurements are traditionally based on the MF method (Frankenberg et al., 2016). In this method, the background spectra are assumed to be distributed as a multivariate Gaussian $\mathcal{N}$ with covariance matrix $\boldsymbol{\Sigma}$ and background mean radiance $\boldsymbol{\mu}$. If H_0 is a scenario without CH_4 enhancement and H_1 is one with CH_4 enhancement, the MF approach is equivalent to a hypothesis test between the two scenarios:

$$H_0: L_{\mathrm{m}} \sim \mathcal{N}(\boldsymbol{\mu}, \boldsymbol{\Sigma}) \tag{1}$$

$$H_1: L_{\mathrm{m}} \sim \mathcal{N}(\boldsymbol{\mu} + \boldsymbol{t}\alpha, \boldsymbol{\Sigma}) \tag{2}$$

where L_{m} is the measurement radiance; $\boldsymbol{t}$ is the target signature, which is defined in Equation (4); α is the enhancement value, denoting a scaling factor for the target signature that perturbs the background $\boldsymbol{\mu}$. If $\boldsymbol{x}$ is a vector of measurement spectra with one element per wavelength, $\alpha(\boldsymbol{x})$ can be written, based on maximum likelihood estimates (Manolakis et al., 2014), as follows:

$$\alpha(\boldsymbol{x}) = \frac{(\boldsymbol{x} - \boldsymbol{\mu})^T \boldsymbol{\Sigma}^{-1} \boldsymbol{t}}{\boldsymbol{t}^T \boldsymbol{\Sigma}^{-1} \boldsymbol{t}} \tag{3}$$

We utilize the same definitions as in Frankenberg et al. (2016). Specifically, the enhancement value $\alpha(\boldsymbol{x})$ denotes the thickness and concentration within a volume of equivalent absorption, and has units of ppm × m. The target signature $\boldsymbol{t}$ refers to the derivative of the change in measured radiance with respect to a change in absorption path length due to an optically thin absorbing layer of CH_4. Note that this definition has the disadvantage that the accuracy of the result degrades when the absorption is strong and further attenuation becomes nonlinear. At a particular wavelength λ, $\boldsymbol{t}$ can be expressed as:

$$\boldsymbol{t}(\lambda) = -\kappa(\lambda)\boldsymbol{\mu}(\lambda), \quad (4)$$

where κ is the absorption coefficient for a near-surface plume with units of $\mathrm{ppm}^{-1}\,\mathrm{m}^{-1}$. This is different from the units of $\mathrm{m}^2 \cdot \mathrm{mol}^{-1}$ traditionally used for the absorption coefficient κ_{trad} in trace gas remote sensing. Using the ideal gas law to express the volume V (in liters) occupied by one mole of CH_4 at the temperature and pressure corresponding to the plume altitude (V = 22.4 at standard temperature and pressure), and the relations 1 liter = 10^{-3} m^3 and 1 ppm = 10^{-6}, we obtain the following expression for unit conversion (units in parentheses):

$$\kappa_{trad}\ [\mathrm{m}^2 \cdot \mathrm{mol}^{-1}] = \kappa\ [\mathrm{ppm}^{-1}\mathrm{m}^{-1}] \times V\ [\mathrm{liter\ mol}^{-1}] \times 10^{-3}\ [\mathrm{m}^3\ \mathrm{liter}^{-1}] \,/\, 10^{-6}\ [\mathrm{ppm}^{-1}] \quad (5)$$

Figure 1 shows the target signature, which is calculated based on HITRAN absorption cross-sections (Rothman et al., 2009). The background mean radiance $\boldsymbol{\mu}$ used in Equation 4 is based on the AVIRIS-NG measurement shown in Figure 2; this is described in more detail in Section 3.

2.2 OE method

The OE method is widely used for the remote sensing retrieval of satellite measurements, such as from the Orbiting Carbon Observatory-2 (OCO-2; O'Dell et al., 2018), the Spinning Enhanced Visible and Infra-Red Imager (SEVIRI; Merchant et al., 2013), and the Greenhouse Gases Observing Satellite (GOSAT; Yoshida et al., 2013). It combines an explicit (typically nonlinear) forward model of the atmospheric state, a (typically Gaussian) prior probability distribution for the variabilities and a (typically Gaussian) distribution for the spectral measurement errors. In addition, the Bayesian framework used by the OE approach allows new information (from measurements) to be combined with existing information (e.g., from models). In many applications, the forward model is nonlinear, and obtaining the optimal solution requires iterative techniques such as the Levenberg–Marquardt method (Rodgers, 2000), which has been routinely applied to study the impacts of measurement parameters on the retrieval process (see, e.g., Zhang et al., 2015). The iteration in this algorithm follows the below procedure.

$$\mathbf{x_{i+1}} = \mathbf{x_i} + [(1+\gamma)\mathbf{S_a^{-1}} + \mathbf{K_i^T S_\epsilon^{-1} K_i}]^{-1}\{\mathbf{K_i^T S_\epsilon^{-1}}[\mathbf{y} - \mathbf{F}(\mathbf{x_i})] - \mathbf{S_a^{-1}}[\mathbf{x_i} - \mathbf{x_a}]\} \quad (6)$$

where $\mathbf{x}$ is a state vector of surface and atmospheric properties, $\mathbf{S_a}$ is the *a priori* covariance matrix, $\mathbf{S_\epsilon}$ is the spectral radiance noise covariance matrix, $\mathbf{K}$ is the Jacobian matrix, $\mathbf{x_a}$ is the *a priori* state vector and γ is a parameter determining the size of each iteration step. The measured spectral radiance is denoted

as **y**; **F**(**x**) is the simulated radiance obtained from the forward model. For the retrieval of CH_4 from AVIRIS-NG measurements, the state vector includes the total column amounts of CH_4 and H_2O, while for the retrievals from synthetic spectra, the H_2O concentration is fixed and the state vector only includes the CH_4 total column. The *a priori* values are within 10% of the true values; *a priori* errors are assumed to be 20% for all state vector elements. The retrieved results are shown as the column averaged mixing ratio (XCH_4, in ppm). Aerosols are not included in the state vector for both the real and synthetic retrievals. They are, however, considered in the forward model for the synthetic simulations. Table 1 (WCRP, 1986) lists optical properties for four basic aerosol types (dust, water soluble, oceanic and soot). Table 2 (WCRP, 1986) shows the corresponding properties for three aerosol models that are defined as mixtures of the basic components from Table 1. We employ the Henyey-Greenstein phase function (Henyey and Greenstein, 1941), where aerosol composition is determined by two parameters: single scattering albedo (SSA) and asymmetry parameter (g). The surface albedo is also not retrieved; for both real and synthetic retrievals, it is held fixed and assumed to be independent of wavelength.

3 Detection and retrieval of CH_4 from AVIRIS-NG measurements

To illustrate the OE retrieval and its difference from the MF method, we perform retrievals for an AVIRIS-NG measurement made on 4 September 2014 (ang20140904t204546) in Bakersfield, CA, as shown in Figure 2. The location is to the west of the Kern Front Oil field. This detection is a case study from the NASA/ESA CO_2 and MEthane eXperiment (COMEX) campaign in California during June and August/September 2014, which includes airborne *in situ*, airborne non-imaging remote sensing, and ground-based *in situ* instruments to provide a real-time remote detection and measurement for CH_4 plumes released from anthropogenic sources. An RGB image of flight data is displayed in Figure 2a; the emission source is a pump jack, as described in Thompson et al. (2015). Figure 2b presents results from the MF method, which shows that the CH_4 plume disperses downwind and has a maximum enhancement value of about 2800 ppm × m. Some artifacts caused by surfaces with strong absorption in the 2100–2500 nm wavelength range, such as oil-based paints or roofs with calcite as a component (Thorpe et al., 2013), also produce large α values in the MF method; these can be removed by an optimization method such as the column-wise MF technique (Thompson et al., 2015).

Figure 3 displays the measured radiance (a) before normalization and (b) after normalization, corresponding to two detector elements (in plume and out of plume). Every element is a cross-track spatial location. The normalization is done by calculating the ratio of the radiance to the maximum value across the spectral range, such that the values fall between 0 and 1. This is a first order correction for the effects of surface albedo. Comparing the measured spectrum in plume to that out of plume, there is

obvious enhancement of CH_4 that is particularly evident in the normalized radiance. CH_4 is the main absorber in the 2100–2500 nm wavelength range, and H_2O is the major interfering gas. Figure 3b indicates the absorption peaks due to H_2O and CH_4.

We choose the plume center with 500 elements to illustrate results obtained using the MF and OE methods. The former evaluates the CH_4 α value compared to the background CH_4 concentration, while the latter retrieves XCH_4. In the MF method, the background covariance matrix $\mathbf{\Sigma}$ and mean radiance $\boldsymbol{\mu}$ are drawn from a reference region close to the CH_4 emission source. These are shown in Figure 2, where the dashed green box denotes the reference region and the source is located within the solid red box. In the OE method, results are shown as a multiplicative scaling factor compared to a typical XCH_4 background of 1.822 ppm. This value is the globally averaged marine surface annual mean for 2014 (Ed Dlugokencky, NOAA/GML, www.esrl.noaa.gov/gmd/ccgg/trends_ch4/), the year corresponding to the AVIRIS-NG measurement being studied. We use an accurate and numerically efficient two-stream-exact-single-scattering (2S-ESS) RT model (Spurr and Natraj, 2011). This forward model is different from a typical two-stream model in that the two-stream approximation is used only to calculate the contribution of multiple scattering to the radiation field. Single scattering is treated in a numerically exact manner using all moments of the phase function. This model has been used for remote sensing of greenhouse gases and aerosols (Xi et al., 2015; Zhang et al., 2015, 2016; Zeng et al., 2017, 2018). Aerosols are neither included in the forward model nor retrieved in this analysis. The surface albedo is set to a wavelength-independent value of 0.5.

Results from the two retrieval methods reveal a similar CH_4 plume shape (Figure 4), especially for elements with high CH_4 enhancement. However, larger differences in CH_4 concentrations are evident in the OE retrievals (Figure 4b). Since radiance normalization reduces the impact of surface albedo and aerosols are not included in either retrieval, this might be due to the fact that, in the OE method, H_2O and CH_4 are simultaneously retrieved; the CH_4 retrieval has added uncertainty due to overlapping absorption features between these two gases. The large maximum value of about 3000 in the MF method also contributes to a reduction in relative contrast. While these results provide heuristic information about the relative performance of the two retrieval techniques, it is difficult to compare the CH_4 enhancement directly between the two methods since the background CH_4 concentration used in the MF method cannot be quantified exactly. Further, evaluating retrieval biases due to ignoring aerosol scattering is not trivial when real measurements are used. Therefore, we simulate synthetic spectra (see section 4) using the 2S-ESS RT model to study the impacts of aerosol scattering as a function of different geophysical parameters by varying them in a systematic manner.

4 Aerosol impact analysis

4.1 Synthetic spectra

In a real AVIRIS-NG observation, the exact column concentration of CH_4 cannot be controlled. However, synthetic simulations allow us to manipulate parameters such as CH_4 concentration, surface albedo, AOD, *g*, and SSA, and thereby test aerosol impacts on CH_4 retrievals. The 2S-ESS RT model is used to simulate the AVIRIS-NG spectral radiance. In this model, a prior atmospheric profile with 70 layers from the surface up to 70 km is derived from National Center for Environmental Prediction reanalysis data (Kalnay et al., 1996); absorption coefficients for all relevant gases are obtained from the HITRAN database (Rothman et al., 2009). Monochromatic RT calculations are performed at a spectral resolution of 0.5 cm^{-1}; the radiance spectrum is then convolved using a Gaussian instrument line shape function with a wavelength-dependent full width at half maximum (FWHM) from a calibrated AVIRIS-NG data file. The signal to noise ratio (SNR) is set to be 300, with Gaussian white noise added. This procedure results in a wavelength grid with a resolution of about 5 nm. The spectral wavelength range used to retrieve CH_4 is from 2100 nm to 2500 nm.

The additional atmospheric and geometric variables included in the model are listed in Table 3, which are held constant unless otherwise mentioned. The observation geometry parameters are taken from a real AVIRIS-NG measurement. Recent AVIRIS-NG fight campaigns have sensor heights ranging from 0.43 to 3.8 km; we choose a value of 1 km, the same as the highest level where aerosol is present in our simulations. The influence of AOD on CH_4 retrieval as a function of SSA and *g* is analyzed in Section 4.3; in all other cases, SSA and *g* are held constant at 0.95 and 0.75, respectively, which is representative of aerosols in the Los Angeles region (Zhang et al., 2015).

4.2 Aerosol impact in the MF method

We simulate synthetic spectra at different AOD, surface albedo and CH_4 concentration values, use the MF method to obtain the CH_4 enhancement, and compare differences in α between scenarios without and with aerosol. The covariance matrix and background mean radiance are calculated from a simulated zero AOD background with surface albedos from 0.1 to 0.5, and XCH_4 set at the typical background value of 1.822 ppm used in Section 3. Figure 5a shows the enhancement value as a function of XCH_4. As the CH_4 concentration increases, the enhancement value obtained by the MF method at first increases approximately linearly. However, the absorption changes in a nonlinear fashion with concentration, whereas the MF method applies a linear formalism to the change. Therefore, the enhancement value (which is correlated with the absorption signature) also shows a deviation from linear behavior at larger XCH_4. Two aerosol scenarios (AOD = 0, 0.3) are compared in Figure 5a, which reveals that the effect of aerosol loading is similar to an underestimation of CH_4 in the retrieval. The underestimation, which is

due to the shielding of CH_4 absorption below the aerosol layer and the fact that multiple scattering effects between the aerosol and the surface are ignored, is clearly shown in Figure 5b, where the enhancement value for fixed CH_4 concentration (same concentration as the background) decreases from 0 ppm × m to −1532 ppm × m with increasing AOD. To clarify the impact of AOD at different surface albedo values, zoomed in versions of α as a function of XCH_4 are presented in Figures 5c–f. For the AOD = 0 scenario, the results are independent of surface albedo. This is because there are no multiple scattering effects between the surface and the atmosphere (Rayleigh scattering is negligible in the retrieval wavelength range) when there is no aerosol loading. For the scenarios with aerosol loading, the dispersion in the zero-enhancement XCH_4 value between different surface albedos indicates that results from the MF method are biased more at large AOD and surface albedo values (Figures 5d–f). This is a consequence of increased multiple scattering between the aerosol layer and the surface that is not accounted for by the retrieval algorithm. The maximum bias value is close to − 700 ppm × m (equivalent to − 0.06 × 1.822 ppm relative to the background concentration of 1.0 × 1.822 ppm) for an AOD of 0.3 and surface albedo of 0.5 (Figure 5f). The implication of these results is that accurate knowledge of the surface albedo is important for MF retrievals, especially when the aerosol loading is large.

A quantitative analysis of underestimation of CH_4 concentration due to aerosol scattering is presented in Figure 6. The color bar shows the α bias — which is defined as the difference between the enhancement value without aerosol (true α value) and that with aerosol — for different CH_4 concentrations, surface albedos and AODs. A positive bias means that CH_4 is underestimated. The α bias increases with increasing surface albedo and AOD, reaching a maximum value of about 700 ppm × m for the simulated cases. However, it is interesting that the bias decreases with increasing CH_4 concentration, which is different from the results obtained by the OE method (discussed in Section 4.3). This surprising behavior is a direct consequence of the physical basis of the MF method. The rate of increase in enhancement becomes smaller as XCH_4 becomes larger (Figure 5a). Therefore, at higher XCH_4 values, the addition of aerosols (which has a similar effect as a reduction in XCH_4) results in a lower reduction in enhancement compared to that at lower XCH_4 values, resulting in a net decrease in the enhancement bias.

4.3 Aerosol impact in the OE method

For the simulation of the synthetic spectra, we assume nonzero aerosol loading below 1 km elevation. The OE method is then used to perform retrievals using the same configuration (including, in particular, the same surface albedo) except that AOD is set to zero. This approach is similar to neglecting aerosol scattering in the CH_4 retrieval; the retrieval bias is defined as the difference between the true XCH_4 in the simulation and the retrieved value (positive values refer to underestimation). First, we study the

306 retrieval bias caused by different aerosol types and mixtures. Figure 7a shows CH_4 retrieval biases as a
307 function of SSA and *g*; surface albedo and AOD are kept constant at 0.3 and XCH_4 is assumed to be 1.0
308 × 1.822 ppm. The retrieval bias increases with SSA and decreases with *g*, with a maximum bias ratio
309 (ratio of retrieval bias to the true value) of about 20%. This behavior can be explained as follows. At
310 higher SSA values, there are more multiple scattering effects (that are ignored in the retrieval). On the
311 other hand, larger values of *g* imply greater anisotropy of scattering (preference for forward scattering),
312 leading to a reduction in multiple scattering effects. Since the retrieval bias is large for high SSA and
313 low *g*, the water-soluble aerosol type (Table 1) and the maritime aerosol model (Table 2) can be expected
314 to induce greater biases in the retrieval. In order to compare the impacts of SSA and *g* in further detail,
315 retrieval results due to a ± 5% change in SSA and *g* for the three aerosol models from Table 2 are shown
316 in Figures 7b and 7c. Note that for the maritime aerosol model, the SSA is set to 0.999 for the +5%
317 scenario to ensure physicality. It is clear that (1) the maritime aerosol model induces larger retrieval
318 biases than the other aerosol types, and (2) the retrieval results are more sensitive to changes in *g* than
319 those in SSA.
320 We then simulate synthetic spectra for different values of CH_4 concentration, surface albedo and
321 AOD. The impacts of aerosol scattering on the retrievals for these scenarios are demonstrated in Figure
322 8. Figure 8a shows a 5 × 5 panel of boxes. Within each box, XCH_4 is constant, while surface albedo
323 increases from top to bottom and AOD increases from left to right. The variation of XCH_4 across the
324 boxes is shown in Figure 8b. We also show a zoomed in plot of the bottom right box (XCH_4 = 5.8 ×
325 1.822 ppm) in Figure 8c, which illustrates the AOD and surface albedo changes within a box. These
326 changes are identical for all boxes. Figure 8a indicates that OE retrievals produce larger CH_4 biases at
327 higher XCH_4 values, in contrast with MF results. In addition, it is evident that the retrieved CH_4 bias
328 increases with increasing AOD. The CH_4 bias induced by differences in the surface albedo is not as large
329 as that due to AOD variations, but surface albedo effects are noticeable at large AOD. Figure 8d shows
330 the sensitivity of retrieval biases to changes in AOD and surface albedo, again demonstrating the greater
331 impact of AOD than surface albedo in the retrieval.
332 The effects of changing the *a priori*, *a priori* error and RT simulation spectral resolution on the
333 retrieved XCH_4 are shown in Figure 9. For these calculations, the other parameters are set as follows:
334 SSA = 0.95, *g* = 0.75, AOD = 1.0, surface albedo = 0.5 and true XCH_4 = 5.8 × 1.822ppm. The parameters
335 were chosen to correspond to the scenario with the largest retrieval bias in Figure 8c (bottom right box
336 in Figure 8c). Figure 9a shows that the retrieved XCH_4 changes by about 9 ppb as the *a priori* changes
337 from half to twice the true XCH_4 value. Similarly, the XCH_4 difference is less than 4 ppb when the *a*
338 *priori* error changes from 0.05 to 0.5 (Figure 9b). Compared to the bias of about 923 ppb induced by

neglecting aerosol scattering for this scenario, it is clear that the impacts of the *a priori* and *a priori* error are very small. The effect of spectral resolution is larger, but XCH_4 still changes by only about 100 ppb when the spectral resolution is changed from 0.5 to 0.1 cm^{-1} (Figure 9c).

4.4 Comparison of the two retrieval techniques

Figure 10 presents the bias ratios for the two retrieval techniques at different AODs (surface albedo = 0.3). In the MF method, the bias ratio is defined as the ratio of the bias to the true value of α. On the other hand, in the OE method, it is the ratio of the bias to the true XCH_4. From Figure 10 it is clear that the bias ratio decreases with increasing CH_4 concentration and has higher values at larger AODs. The bias ratio for the MF method (1.3–4.5%) is up to 53.6% less than that for the OE method (2.8–5.6%) for AOD = 0.3 when the CH_4 concentration is high (2–5 times typical background values). On the other hand, the OE method performs better when enhancements are small and XCH_4 is close to the background value. For example, the bias ratio for the MF method has a high value of about 42.6% at AOD = 0.3 for a 10% enhancement ($XCH_4 = 1.1 \times 1.822$ ppm); the OE value for the same scenario is 8.6%. For scenarios where scattering is ignored, the two retrieval techniques seem to be complementary, with differing utilities for different enhancements. On the other hand, when RT models that account for scattering effects are employed, the MF technique is suboptimal. Further, MF retrievals rely on accurate characterization of the surface albedo, especially when the aerosol loading is large. Finally, the MF method does not retrieve concentrations, which are necessary to infer fluxes. Therefore, the OE technique is in general superior due to its ability to support simultaneous retrieval of aerosols, surface albedo and CH_4 concentration.

5 Summary and discussion

Remote sensing measurements from airborne and satellite instruments are widely used to detect CH_4 emissions. In our study, the traditional MF and the OE methods are used to quantify the effects of aerosol scattering on CH_4 retrievals based on simulations of AVIRIS-NG measurements. The results show that the retrieval biases increase with increasing AOD and surface albedo for both techniques. In the OE method the biases increase with increasing CH_4 concentration and SSA, but decrease with increasing aerosol asymmetry parameter. The CH_4 retrieval bias increases with increasing XCH_4 in the OE method but decreases for the same scenario in the MF method. The surprising MF trend is attributed to the inability of the MF method to treat nonlinear absorption effects at high XCH_4 values. We also present bias ratios for the two techniques. The MF method shows smaller bias ratios at large CH_4 concentrations than the OE method; it is, therefore, the optimal method to detect strong CH_4 emission sources when scattering effects can be ignored in the retrieval. For the same retrieval scenario, the OE

method seems to be more suitable for detecting diffuse sources. Further, the MF method relies on a comparison with the background CH_4 concentration. It is difficult to get an accurate estimate of the background XCH_4 value in polluted atmospheric environments. In contrast, the OE method provides retrievals based solely on the atmospheric scenario of interest; CH_4, aerosols and surface albedo can be simultaneously inferred. Therefore, when scattering effects need to be considered, the OE method is the appropriate choice. Indeed, the MF method was intended for plume detection. OE enables accurate quantification of XCH_4 in the presence of aerosol scattering.

This study focused on a comparison of retrieval techniques. It is also important to accurately represent the physics of atmospheric RT, especially for scenarios with significant aerosol scattering. RT models traditionally used in retrievals of imaging spectroscopic data use simplified radiation schemes and predefined aerosol models, which may introduce inaccurate in the representation of atmospheric physics. The 2S-ESS model provides the capability to quantify aerosol impacts on CH_4 retrieval for different aerosol types, optical depths and layer heights. In future work, we will compare retrievals using the 2S-ESS model against those from other commonly used models such as MODTRAN. We will also evaluate the impact of varying instrument spectral resolution and signal to noise ratio for simultaneous retrieval of CH_4, surface albedo and AOD. This will be relevant for the design of imaging spectrometers for planned future missions such as the NASA Surface Biology and Geology (SBG) mission.

Data availability

The code and data are available from the authors upon request.

Author contributions

VN conceived the work, provided the radiative transfer and aerosol models, supervised YH, and assisted with manuscript preparation. YH designed and performed the retrievals, analyzed the results, and prepared the original manuscript. ZZ contributed to retrieval setup and assisted with analysis of the results. PK provided valuable inputs into the science of CH_4 remote sensing. YLY supervised YH and participated in the evaluation of the retrieval results and intercomparison. All listed authors contributed to the review and editing of this manuscript.

Competing interests

The authors declare that they have no conflict of interest.

Acknowledgements

A portion of this research was carried out at the Jet Propulsion Laboratory, California Institute of Technology, under a contract with the National Aeronautics and Space Administration (80NM0018D0004). The authors gratefully acknowledge the insightful and constructive comments from the two anonymous reviewers, which improved the clarity and quality of the manuscript, and elevated the significance of the work beyond the original expectation.

Financial Support

VN acknowledges support from the NASA "Utilization of Airborne Visible/Infrared Imaging Spectrometer Next Generation Data from an Airborne Campaign in India" program (solicitation NNH16ZDA001N-AVRSNG), and the Jet Propulsion Laboratory Research and Technology Development program. PK was funded by the Japan Society for the Promotion of Science International Research Fellow Program.

References

Alvarez, R. A., Zavala-Araiza, D., Lyon, D. R., Allen, D. T., Barkley, Z. R., Brandt, A. R., Davis, K. J., Herndon, S. C., Jacob, D. J., Karion, A., Kort, E. A., Lamb, B. K., Lauvaux, T., Maasakkers, J. D., Marchese, A. J., Omara, M., Pacala, S. W., Peischl, J., Robinson, A. L., Shepson, P. B., Sweeney, C., Townsend-Small, A., Wofsy, S. C., and Hamburg, S. P.: Assessment of methane emissions from the U.S. oil and gas supply chain, Science, 361, 186–188, https://doi.org/10.1126/science.aar7204, 2018.

Archer, D.: Methane hydrate stability and anthropogenic climate change, Biogeosci., 4, 521–544, https://doi.org/10.5194/bg-4-521-2007, 2007.

Bradley, E. S., Leifer, I., Roberts, D. A., Dennison, P. E., and Washburn, L.: Detection of marine methane emissions with AVIRIS band ratios, Geophys. Res. Lett., 38, L10702, https://doi.org/10.1029/2011GL046729, 2011.

Bubier, J. L., and Moore, T. R: An ecological perspective on methane emissions from northern wetlands, Trends in Ecology and Evolution, 9, 460–464, https://doi.org/10.1016/0169-5347(94)90309-3, 1994.

Buchwitz, M., Reuter, M., Bovensmann, H., Pillai, D., Heymann, J., Schneising, O., Rozanov, V., Krings, T., Burrows, J. P., Boesch, H., Gerbig, C., Meijer, Y., and Löscher, A.: Carbon Monitoring Satellite (CarbonSat): Assessment of atmospheric CO_2 and CH_4 retrieval errors by error parameterization, Atmos. Meas. Tech., 6, 3477–3500, https://doi.org/10.5194/amt-6-3477-2013, 2013.

Butz, A., Galli, A., Hasekamp, O., Landgraf, J., Tol, P., and Aben, I.: TROPOMI aboard Sentinel-5 Precursor: Prospective performance of CH_4 retrievals for aerosol and cirrus loaded atmospheres, Remote Sens. Environ., 120, 267–276, https://doi.org/10.1016/j.rse.2011.05.030, 2012.

Butz, A., Orphal, J., Checa-Garcia, R., Friedl-Vallon, F., von Clarmann, T., Bovensmann, H., Hasekamp, O., Landgraf, J., Knigge, T., Weise, D., Sqalli-Houssini, O., and Kemper, D.: Geostationary Emission Explorer for Europe (G3E): Mission concept and initial performance assessment, Atmos. Meas. Tech., 8, 4719–4734, https://doi.org/10.5194/amt-8-4719-2015, 2015.

Clerbaux, C., Hadji-Lazaro, J., Turquety, S., Mégie, G., and Coheur, P.-F.: Trace gas measurements from infrared satellite for chemistry and climate applications, Atmos. Chem. Phys., 3, 1495–1508, https://doi.org/10.5194/acp-3-1495-2003, 2003.

Dennison, P. E., Thorpe, A. K., Pardyjak, E. R., Roberts, D. A., Qi, Y., Green, R. O., Bradley, E. S., and Funk, C. C.: High spatial resolution mapping of elevated atmospheric carbon dioxide using airborne imaging spectroscopy: Radiative transfer modeling and power plant plume detection, Remote Sens. Environ., 139, 116-129, https://doi.org/10.1016/j.rse.2013.08.001, 2013.

Etiope, G., Feyzullayev, A., and Baciu, C. L.: Terrestrial methane seeps and mud volcanoes: A global perspective of gas origin, Mar. Pet. Geol., 26, 333–344, https://doi.org/10.1016/j.marpetgeo.2008.03.001, 2009.

Fishman, J. L., Iraci, L. T., Al-Saadi, J., Chance, K., Chavez, F., Chin, M., Coble, P., Davis, C., DiGiacomo, P. M., Edwards, D., Eldering, A., Goes, J., Herman, J., Hu, C., Jacob, D. J., Jordan, C., Kawa, S. R., Key, R., Liu, X., Lohrenz, S., Mannino, A., Natraj, V., Neil, D., Neu, J., Newchurch, M., Pickering, K., Salisbury, J., Sosik, H., Subramaniam, A., Tzortziou, M.,Wang, J., and Wang, M.: The United States' next generation of atmospheric composition and coastal ecosystem measurements: NASA's Geostationary Coastal and Air Pollution Events (GEO-CAPE) Mission, Bull. Am. Meteorol. Soc., https://doi.org/10.1175/BAMS-D-11-00201.1, 2012.

Frankenberg, C., Platt, U., and Wagner, T.: Iterative maximum a posteriori (IMAP)-DOAS for retrieval of strongly absorbing trace gases: Model studies for CH_4 and CO_2 retrieval from near infrared spectra of SCIAMACHY onboard ENVISAT, Atmos. Chem. Phys., 5, 9–22, https://doi.org/10.5194/acp-5-9-2005, 2005.

Frankenberg, C., Meirink, J. F., Bergamaschi, P., Goede, A., P. H., Heimann, M., Körner, S., Platt, U., van Weele, M., and Wagner, T.: Satellite chartography of atmospheric methane from SCIAMACHY on board ENVISAT: Analysis of the years 2003 and 2004, J. Geophys. Res., 111, D07303, https://doi.org/10.1029/2005JD006235, 2006.

Frankenberg, C., Thorpe, A. K., Thompson, D. R., Hulley, G., Kort, E. A., Vance, N., Borchardt, J., Krings, T., Gerilowski, K., Sweeney, C., Conley, S., Bue, B. D., Aubrey, A. D., Hook, S., and Green, R.

O.: Airborne methane remote measurements reveal heavy-tail flux distribution in Four Corners region, Proc. Natl. Acad. Sci. U. S. A., 113, 9734–9739, https://doi.org/10.1073/pnas.1605617113, 2016.

Gambacorta, A., Barnet, C. D., Smith, N., Pierce, R. B., Smith, J. W., Spackman, J. R., and Goldberg, M.: The NPP and J1 NOAA Unique Combined Atmospheric Processing System (NUCAPS) for atmospheric thermal sounding: Recent algorithm enhancements tailored to near real time users applications, Abstract IN33D-07, presented at 2016 Fall Meeting, AGU, San Francisco, CA, 12–16 Dec., 2016.

Gedney, N., Cox, P. M., and Huntingford, C.: Climate feedback from wetland methane emissions, Geophys. Res. Lett., 31, L20503. https://doi.org/10.1029/2004GL020919, 2004.

Glumb, R., Davis, G., and Lietzke, C.: The TANSO-FTS-2 instrument for the GOSAT-2 greenhouse gas monitoring mission, 2014 IEEE Geoscience and Remote Sensing Symposium, Quebec City, QC, 1238–1240, https://doi.org/10.1109/IGARSS.2014.6946656, 2014.

Green, R. O., Eastwood, M. L., Sarture, C. M., Chrien, T. G., Aronsson, M., Chippendale, B. J., Faust, J. A., Pavri, B. E., Chovit, C. J., Solis, M., Olah, M. R., and Williams, O.: Imaging spectroscopy and the Airborne Visible/Infrared Imaging Spectrometer (AVIRIS), Remote Sens. Environ., 65, 227–248, https://doi.org/10.1016/S0034-4257(98)00064-9, 1998.

He, L., Zeng, Z.-C., Pongetti, T. J., Wong, C., Liang, J., Gurney, K. R., Newman, S., Yadav, V., Verhulst, K., Miller, C. E., and Duren, R.: Atmospheric methane emissions correlate with natural gas consumption from residential and commercial sectors in Los Angeles, Geophys. Res. Lett., 46, 8563–8571, https://doi.org/10.1029/2019GL083400, 2019.

Henyey, L. G., and Greenstein, J. L.: Diffuse radiation in the galaxy, Astrophys. J., 93, 70–83, https://doi.org/10.1086/144246, 1941.

Herrero, M., Henderson, B., Havlík, P., Thornton, P. K., Conant, R. T., Smith, P., Wirsenius, S., Hristov, A. N., Gerber, P., Gill, M., Butterbach-Bahl, K., Valin, H., Garnett, T., and Shehfest, E.: Greenhouse gas mitigation potentials in the livestock sector, Nature Clim. Change, 6, 452–461, https://doi.org/10.1038/nclimate2925, 2016.

Holmes, C. D., Prather, M. J., Søvde, O. A., and Myhre, G.: Future methane, hydroxyl, and their uncertainties: key climate and emission parameters for future predictions, Atmos. Chem. Phys., 13, 285–302, https://doi.org/10.5194/acp-13-285-2013, 2013.

Howarth, R. W.: Methane emissions and climatic warming risk from hydraulic fracturing and shale gas development: implications for policy, Energy and Emission Control Technologies, 3, 45–54, https://doi.org/10.2147/EECT.S61539, 2015.

Howarth, R. W.: Ideas and perspectives: is shale gas a major driver of recent increase in global atmospheric methane?, Biogeosciences, 16, 3033–3046, https://doi.org/10.5194/bg-16-3033-2019, 2019.

Howarth, R. W., Santoro, R., and Ingraffea, A.: Methane and the greenhouse gas footprint of natural gas from shale formations, Clim. Change, 106, 679, https://doi.org/10.1007/s10584-011-0061-5, 2011.

Jacob, D. J., Turner, A. J., Maasakkers, J. D., Sheng, J., Sun, K., Liu, X., Chance, K., Aben, I., McKeever, J., and Frankenberg, C.: Satellite observations of atmospheric methane and their value for quantifying methane emissions, Atmos. Chem. Phys., 16, 14371–14396, https://doi.org/10.5194/acp-16-14371-2016, 2016.

Jervis, D., McKeever, J., Durak, B. O. A., Sloan, J. J., Gains, D., Varon, D. J., Ramier, A., Strupler, M., and Tarrant, E.: The GHGSat-D imaging spectrometer, Atmos. Meas. Tech. Discuss., https://doi.org/10.5194/amt-2020-301, in review, 2020.

Kalnay, E., Kanamitsu, M., Kistler, R., Collins, W., Deaven, D., Gandin, L., Iredell, M., Saha, S., White, G., Woollen, J., Zhu, Y., Chelliah, M., Ebisuzaki, W., Higgins, W., Janowiak, J., Mo, K. C., Ropelewski, C., Wang, J., Leetmaa, A., Reynolds, R., Jenne, R., and Joseph, D.: The NCEP/NCAR 40-year reanalysis project, Bull. Am. Meteorol. Soc., 77, 437–471, https://doi.org/10.1175/1520-0477(1996)077<0437:TNYRP>2.0.CO;2, 1996.

Kiemle, C., Kawa, S. R., Quatrevalet, M., and Browell, E. V.: Performance simulations for a spaceborne methane lidar mission, J. Geophys. Res., 119, 4365–4379, https://doi.org/10.1002/2013JD021253, 2014.

Kirschke, S., Bousquet, P., Ciais, P., Saunois, M., Canadell, Josep G., Dlugokencky. E. J., Bergamaschi, P., Bergmann, D., Blake, D. R., Bruhwiler, L., Cameron-Smith, P., Castaldi, S., Chevallier, F., Feng, L., Fraser, A., Heimann, M, Hodson, E. L., Houweling, S., Josse, B., Fraser, P. J., Krummel, P. B., Lamarque, J.-F., Langenfelds, R. L., Le Quere, C., Naik, V., O'Doherty, S., Palmer, P. I., Pison, I., Plummer, D., Poulter, B., Prinn, R. G., Rigby, M., Ringeval, B., Santini, M. Schmidt, M., Shindell, D. T., Simpson, I. J., Spahni, R., Steele, L. P., Strode, S. A., Sudo, K., Szopa, S., van der Werf, G. R., Voulgarakis, A., van Weele, M., Weiss, R. F., Williams, J. E., and Zeng, G.: Three decades of global methane sources and sinks, Nature Geosci., 6, 813–823, https://doi.org/10.1038/ngeo1955, 2013.

Kort, E. A., Frankenberg, C., Costigan, K. R., Lindenmaier, R., Dubey, M. K., and Wunch, D.: Four corners: the largest US methane anomaly viewed from space, Geophys. Res. Lett., 41, 6898–6903, https://doi.org/10.1002/2014GL061503, 2014.

Kuze, A., Suto, H., Shiomi, K., Kawakami, S., Tanaka, M., Ueda, Y., Deguchi, A., Yoshida, J., Yamamoto, Y., Kataoka, F., Taylor, T. E., and Buijs, H. L.: Update on GOSAT TANSO-FTS performance, operations, and data products after more than 6 years in space, Atmos. Meas. Tech., 9, 2445–2461, https://doi.org/10.5194/amt-9-2445-2016, 2016.

Kvenvolden, K. A.: Methane hydrate – A major reservoir of carbon in the shallow geosphere, Chem. Geol., 71, 41–51, https://doi.org/10.1016/0009-2541(88)90104-0, 1988.

Kvenvolden, K. A., and Rogers, B. W.: Gaia's breath – global methane exhalations, Mar. Pet. Geol., 22, 579–590, https://doi.org/10.1016/j.marpetgeo.2004.08.004, 2005.

Macdonald, J. A., Fowler, D., Hargreaves, K. J., Skiba, U., Leith, I. D., and Murray, M. B.: Methane emission rates from a northern wetland; response to temperature, water table and transport, Atmos. Environ., 32, 3219–3227, https://doi.org/10.1016/S1352-2310(97)00464-0, 1998.

Manolakis, D., Truslow, E., Pieper, M., Cooley, T., and Brueggeman, M.: Detection algorithms in hyperspectral imaging systems: An overview of practical algorithms, IEEE Signal Proc. Mag., 31, 24–33, https://doi.org/10.1109/MSP.2013.2278915, 2014.

McKeever, J., Durak, B. O. A., Gains, D., Varon, D. J., Germain, S., and Sloan, J. J.: GHGSat-D: Greenhouse gas plume imaging and quantification from space using a Fabry-Perot imaging spectrometer, Abstract A33G-1360 presented at 2017 Fall Meeting, AGU, New Orleans, LA, 11–15 December, 2017.

Merchant, C. J., Le Borgne, P., Roquet, H., and Legendre, G.: Extended optimal estimation techniques for sea surface temperature from the Spinning Enhanced Visible and Infra-Red Imager (SEVIRI), Remote Sens. Environ., 131, 287–297, https://doi.org/10.1016/j.rse.2012.12.019, 2013.

Myhre, G., Shindell, D., Bréon, F.-M., Collins, W., Fuglestvedt, J., Huang, J., Koch, D., Lamarque, J.-F., Lee, D., Mendoza, B., Nakajima, T., Robock, A., Stephens, G., Takemura, T., and Zhang, H.: Anthropogenic and Natural Radiative Forcing, Climate Change 2013: The Physical Science Basis. Contribution of Working Group I to the Fifth Assessment Report of the Intergovernmental Panel on Climate Change – IPCC, 2013.

Nisbet, E. G., Dlugokencky, E, J., and Bousquet, P.: Methane on the rise-Again, Science, 343, 493–495, https//doi.org/10.1126/science.1247828, 2014.

Nisbet, E. G., Dlugokencky, E. J., Manning, M. R., Lowry, D., Fisher, R. E., France, J. L., Michel, S. E., Miller, J. B., White, J. W. C., Vaughn, B., Bousquet, P., Pyle, J. A., Warwick, N. J., Cain, M., Brownlow, R., Zazzeri, G., Lanoisellé, M., Manning, A. C., Gloor, E., Worthy, D. E. J., Brunke, E.-G., Labuschagne, C., Wolff, E. W., and Ganesan, A. L.: Rising atmospheric methane: 2007–2014 growth and isotopic shift, Glob. Biogeochem. Cycles, 30, 1356–1370, https://doi.org/10.1002/2016GB005406, 2016.

NOAA Earth System Research Laboratory Global Monitoring Laboratory, https://esrl.noaa.gov/gmd/ccgg/trends_ch4/, 2019.

O'Dell, C. W., Eldering, A., Wennberg, P. O., Crisp, D., Gunson, M. R., Fisher, B., Frankenberg, C., Kiel, M., Lindqvist, H., Mandrake, L., Merrelli, A., Natraj, V., Nelson, R. R., Osterman, G. B., Payne, V. H., Taylor, T. E., Wunch, D., Drouin, B. J., Oyafuso, F., Chang, A., McDuffie, J., Smyth, M., Baker, D. F., Basu, S., Chevallier, F., Crowell, S. M. R., Feng, L., Palmer, P. I., Dubey, M., García, O. E., Griffith, D. W. T., Hase, F., Iraci, L. T., Kivi, R., Morino, I., Notholt, J., Ohyama, H., Petri, C., Roehl, C. M., Sha, M. K., Strong, K., Sussmann, R., Te, Y., Uchino, O. and Velazco, V. A.: Improved retrievals

of carbon dioxide from Orbiting Carbon Observatory-2 with the version 8 ACOS algorithm, Atmos. Meas. Tech., 11(12), 6539–6576, https://doi.org/10.5194/amt-11-6539-2018, 2018.

Polonsky, I. N., O'Brien, D. M., Kumer, J. B., O'Dell, C. W., and the geoCARB Team: Performance of a geostationary mission, geoCARB, to measure CO_2, CH_4 and CO column-averaged concentrations, Atmos. Meas. Tech., 7, 959–981, https://doi.org/10.5194/amt-7-959-2014, 2014.

Roberts, D. A., Bradley, E. S., Cheung, R., Leifer, I., Dennison, P. E., and Margolis, J. S.: Mapping methane emissions from a marine geological seep source using imaging spectrometry, Remote Sens. Environ., 114, 592–606, https://doi.org/10.1016/j.rse.2009.10.015, 2010.

Rodgers, C. D.: Inverse Methods for Atmospheric Sounding: Theory and Practice, World Scientific, Singapore, 2000.

Rothman, L. S., Gordon, I. E., Barbe, A., Benner, D. C., Bernath, P. E., Birk, M., Boudon, V., Brown, L. R., Campargue, A., Champion, J. P., Chance, K., Coudert, L. H., Dana, V., Devi, V. M., Fally, S., Flaud, J. M., Gamache, R. R., Goldman, A., Jacquemart, D., Kleiner, I., Lacome, N., Lafferty, W. J., Mandin, J. Y., Massie, S. T., Mikhailenko, S. N., Miller, C. E., Moazzen-Ahmadi, N., Naumenko, O. V., Nikitin, A. V., Orphal, J., Perevalov, V. I., Perrin, A., Predoi-Cross, A., Rinsland, C. P., Rotger, M., Šimečková, M., Smith, M. A. H., Sung, K., Tashkun, S. A., Tennyson, J., Toth, R. A., Vandaele, A. C., and Vander Auwera, J.: The HITRAN 2008 molecular spectroscopic database, J. Quant. Spectrosc. Radiat. Transfer, 110, 533–572, https://doi.org/10.1016/j.jqsrt.2009.02.013, 2009.

Schaefer, H., Fletcher, S. E. M., Veidt, C., Lassey, K. R., Brailsford, G. W., Bromley, T. M., Dlugokencky, E. J., Michel, S. E., Miller, J. M., Levin, I., Lowe, D. C., Martin, R. J., Vaughn, B. H., and White, J. W. C.: A 21st-century shift from fossil-fuel to biogenic methane emissions indicated by $^{13}CH_4$, Science, 352, 80-84, https://doi.org/10.1126/science.aad2705, 2016.

Schaefer, K., Lantuit, H., Romanovsky, V. E., Schuur, E. A. G., and Witt, R.: The impact of the permafrost carbon feedback on global climate, Environ. Res. Lett., 9, 085003, https://doi.org/10.1088/1748-9326/9/8/085003, 2014.

644 Schuur, E. A. G., McGuire, A. D., Schädel, C., Grosse, G., Harden, J. W., Hayes, D. J., Hugelius, G.,
645 Koven, C. D., Kuhry, P., Lawrence, D. M., Natali, S. M., Olefeldt, D., Romanovsky, V. E., Schaefer, K.,
646 Turetsky, M. R., Treat, C. C., and Vonk, J. E.: Climate change and the permafrost carbon feedback,
647 Nature, 520, 171–179, https://doi.org/10.1038/nature14338, 2015.
648
649 Seinfeld, J. H., and Pandis, S. N.: Atmospheric Chemistry and Physics: From Air Pollution to Climate
650 Change, Wiley, New Jersey, USA, 2006.
651
652 Spurr, R., and Natraj, V.: A linearized two-stream radiative transfer code for fast approximation of
653 multiple-scatter fields, J. Quant. Spectrosc. Radiat. Transfer, 112, 2630–2637,
654 https://doi.org/10.1016/j.jqsrt.2011.06.014, 2011.
655
656 Themelis, N. J., and Ulloa, P. A.: Methane generation in landfills, Renewable Energy, 32, 1243–1257,
657 https://doi.org/10.1016/j.renene.2006.04.020, 2007.
658
659 Thompson, D. R., Leifer, I., Bovensmann, H., Eastwood, M., Fladeland, M., Frankenberg, C.,
660 Gerilowski, K., Green, R. O., Kratwurst, S., Krings, T., Luna, B., and Thorpe, A. K.: Real-time remote
661 detection and measurement for airborne imaging spectroscopy: a case study with methane, Atmos. Meas.
662 Tech., 8, 4383–4397, https://doi.org/10.5194/amt-8-4383-2015, 2015.
663
664 Thorpe, A. K., Frankenberg, C., and Roberts, D. A.: Retrieval techniques for airborne imaging of
665 methane concentrations using high spatial and moderate spectral resolution: Application to AVIRIS,
666 Atmos. Meas. Tech., 7, 491–506, https://doi.org/10.5194/amt-7-491-2014, 2014.
667 Thorpe, A. K., Roberts, D. A., Bradley, E. S., Funk, C. C., Dennison, P. E., and Leifer, I.: High resolution
668 mapping of methane emissions from marine and terrestrial sources using a Cluster-Tuned Matched Filter
669 technique and imaging spectrometry, Remote Sens. Environ., 134, 305–318,
670 https://doi.org/10.1016/j.rse.2013.03.018, 2013.
671
672 Varon, D. J., McKeever, J., Jervis, D., Maasakkers, J. D., Pandey, S., Houweling, S., Aben, I., Scarpelli,
673 T. and Jacob, D. J.: Satellite discovery of anomalously large methane point sources from oil/gas
674 production, Geophys. Res. Lett., 2019.
675

Veefkind, J. P., Aben, I., McMullan, K., Forster, H., de Vries, J.,Otter, G., Claas, J., Eskes, H. J., de Haan, J. F., Kleipool, Q., van Weele, M., Hasekamp, O., Hoogeveen, R., Landgraf, J., Snel, R., Tol, P., Ingmann, P., Voors, R., Kruizinga, B., Vink, R., Visser, H., and Levelt, P. F.: TROPOMI on the ESA Sentinel-5 Precursor: A GMES mission for global observations of the atmospheric composition for climate, air quality and ozone layer applications, Remote Sens. Environ., 120, 70–83, https://doi.org/10.1016/j.rse.2011.09.027, 2012.

Walter, K. M., Zimov, S. A., Chanton, J. P., Verbyla, D., and Chapin III, F. S.: Methane bubbling from Siberian thaw lakes as a positive feedback to climate warming, Nature, 443, 71–75, https://doi.org/10.1038/nature05040, 2006.

Wofsy, S. C., and Hamburg, S: MethaneSAT — A new observing platform for high resolution measurements of methane and carbon dioxide, Abstract A53F-02 presented at 2019 Fall Meeting, AGU, San Francisco, CA, 9–13 December, 2019.

World Climate Research Program (WCRP): A preliminary cloudless standard atmosphere for radiation computation, International Association for Meteorology and Atmospheric Physics, Radiation Commission, Boulder, CO, USA, 1984, CSP-112, WMO/TD-No. 24, March 1986.

Woodwell, G. M., Mackenzie, F. T., Houghton, R. A., Apps, M., Gorham, E., and Davidson, E.: Biotic feedbacks in the warming of the earth, Climatic Change, 40, 495–518, https://doi.org/10.1023/A:1005345429236, 1998.

Worden, J., Kulawik, S., Frankenberg, C., Payne, V., Bowman, K., Cady-Peirara, K., Wecht, K., Lee, J.-E., and Noone, D.: Profiles of CH_4, HDO, H_2O, and N_2O with improved lower tropospheric vertical resolution from Aura TES radiances, Atmos. Meas. Tech., 5, 397–411, https://doi.org/10.5194/amt-5-397-2012, 2012.

Xi, X., Natraj, V., Shia, R. L., Luo, M., Zhang, Q., Newman, S., Sander, S. P., and Yung, Y. L.: Simulated retrievals for the remote sensing of CO_2, CH_4, CO, and H_2O from geostationary orbit, Atmos. Meas. Tech., 8, 4817–4830, https://doi.org/10.5194/amtd-8-5809-2015, 2015.

Xiong, X., Barnet, C., Maddy, E., Sweeney, C., Liu, X., Zhou, L., and Goldberg, M.: Characterization and validation of methane products from the Atmospheric Infrared Sounder (AIRS), J. Geophys. Res., 113, G00A01, https://doi.org/10.1029/2007JG000500, 2008.

Xiong, X., Barnet, C., Maddy, E. S., Gambacorta, A., King, T. S., and Wofsy, S. C.: Mid-upper tropospheric methane retrieval from IASI and its validation, Atmos. Meas. Tech., 6, 2255–2265, https://doi.org/10.5194/amt-6-2255-2013, 2013.

Yoshida, Y., Kikuchi, N., Morino, I., Uchino, O., Oshchepkov, S., Bril, A., Saeki, T., Schutgens, N., Toon, G. C., Wunch, D., Roehl, C. M., Wennberg, P. O., Griffith, D. W. T., Deutscher, N. M., Warneke, T., Notholt, J., Robinson, J., Sherlock, V., Connor, B., Rettinger, M., Sussmann, R., Ahonen, P., Heikkinen, P., Kyrö, E., Mendonca, J., Strong, K., Hase, F., Dohe, S., and Yokota, T.: Improvement of the retrieval algorithm for GOSAT SWIR XCO_2 and XCH_4 and their validation using TCCON data, Atmos. Meas. Tech., 6, 1533–1547, https://doi.org/10.5194/amt-6-1533-2013, 2013.

Zeng, Z.-C., Zhang, Q., Natraj, V., Margolis, J. S., Shia, R. -L., Newman, S., Fu, D., Pongetti, T. J., Wong, K. W., Sander, S. P., Wennberg, P. O., and Yung, Y. L.: Aerosol scattering effects on water vapor retrievals over the Los Angeles Basin, Atmos. Chem. Phys., 17, 2495–2508, https://doi.org/10.5194/acp-17-2495-2017, 2017.

Zeng, Z.-C., Natraj, V., Xu, F., Pongetti, T. J., Shia, R.-L., Kort, E. A., Toon, G. C., Sander, S. P., and Yung, Y. L.: Constraining aerosol vertical profile in the boundary layer using hyperspectral measurements of oxygen absorption, Geophys. Res. Lett., 45, 10772–10780, https://doi.org/10.1029/2018GL079286, 2018.

Zhang, Q., Natraj, V., Li, K. -F., Shia, R. -L., Fu, D., Pongetti, T. J., Sander S. P., Roehl, C. M., and Yung, Y. L.: Accounting for aerosol scattering in the CLARS retrieval of column averaged CO_2 mixing ratios, J. Geophys. Res., 120, 7205–7218, https://doi.org/10.1002/2015JD023499, 2015.

Zhang, Q., Shia, R. -L., Sander, S. P., and Yung, Y. L.: X_{CO2} retrieval error over deserts near critical surface albedo, Earth Space Sci., 2, 1–10, https://doi.org/10.1002/2015EA000143, 2016.

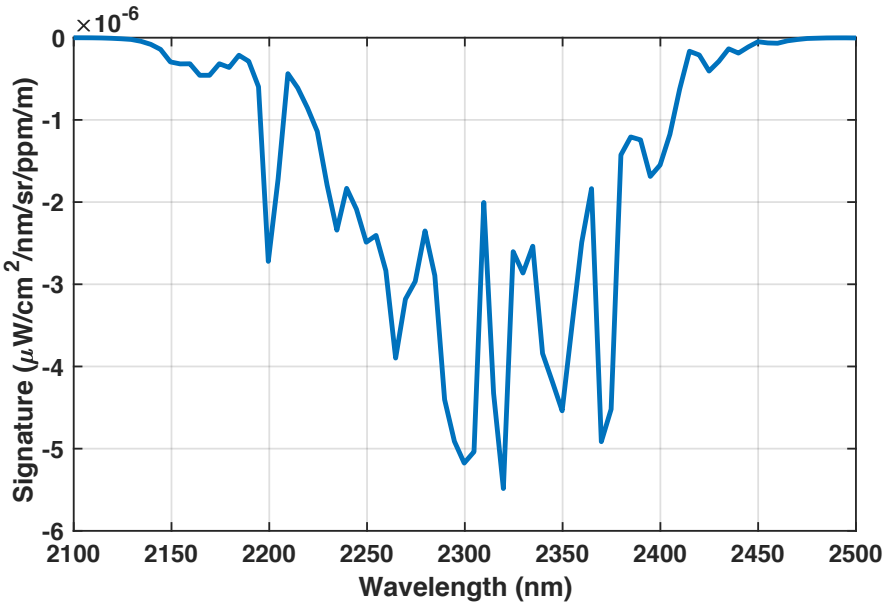

Figure 1: The target signature used for the Matched Filter method.

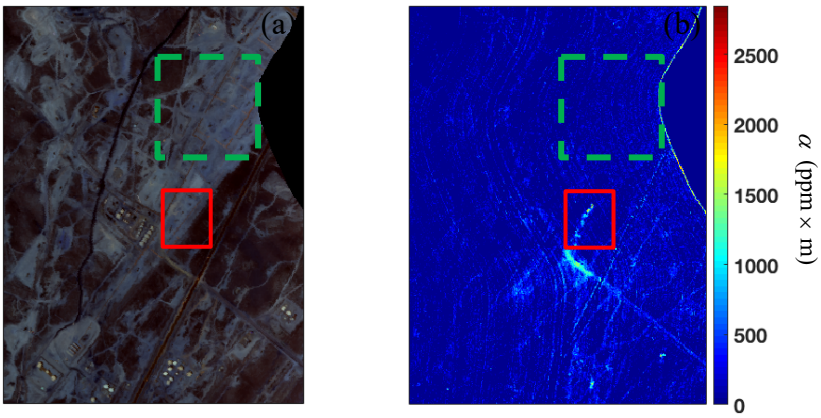

Figure 2: (a) RGB image of flight data from 4 September 2014 (ang20140904t204546). Adapted from Thompson et al. (2015). (b) CH_4 enhancement value α (ppm × m) obtained by the MF method. An emission source is shown in the solid red box and the background region near the target for the MF calculation is indicated by the dashed green box.

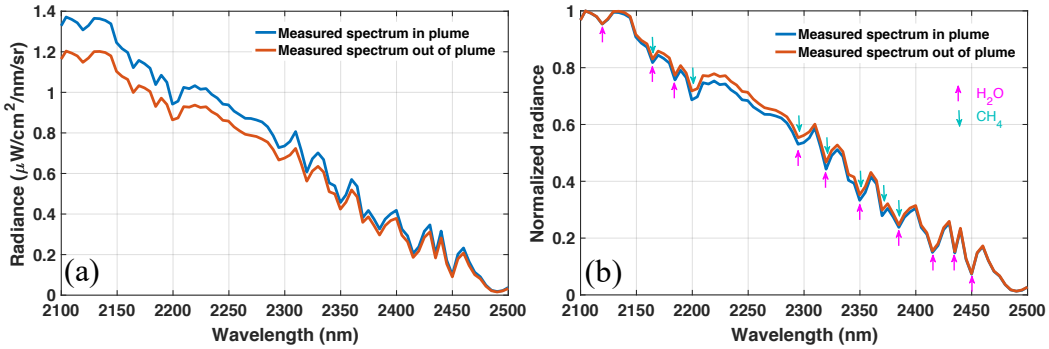

Figure 3: (a) Real radiance and (b) normalized radiance at cross-track detector elements (in and out of plume) from the sample AVIRIS-NG measurement. The colored arrows in (b) show the main absorption features due to H_2O (purple) and CH_4 (green).

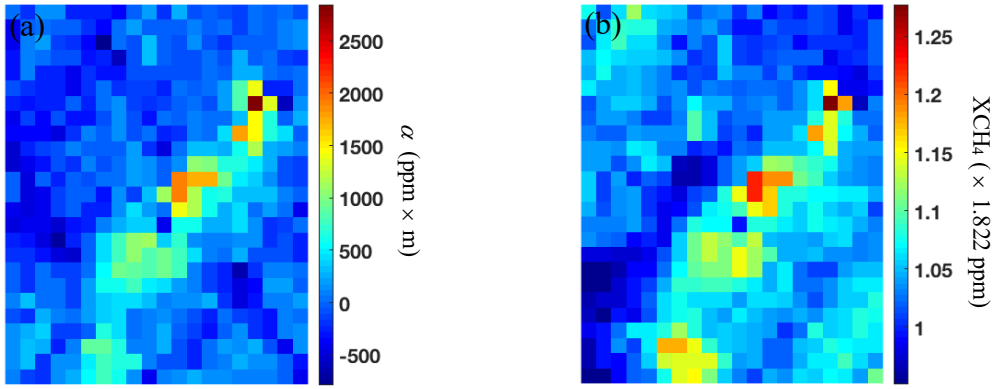

Figure 4: Retrieval image for the plume center (500 elements) based on the (a) MF method and (b) OE method.

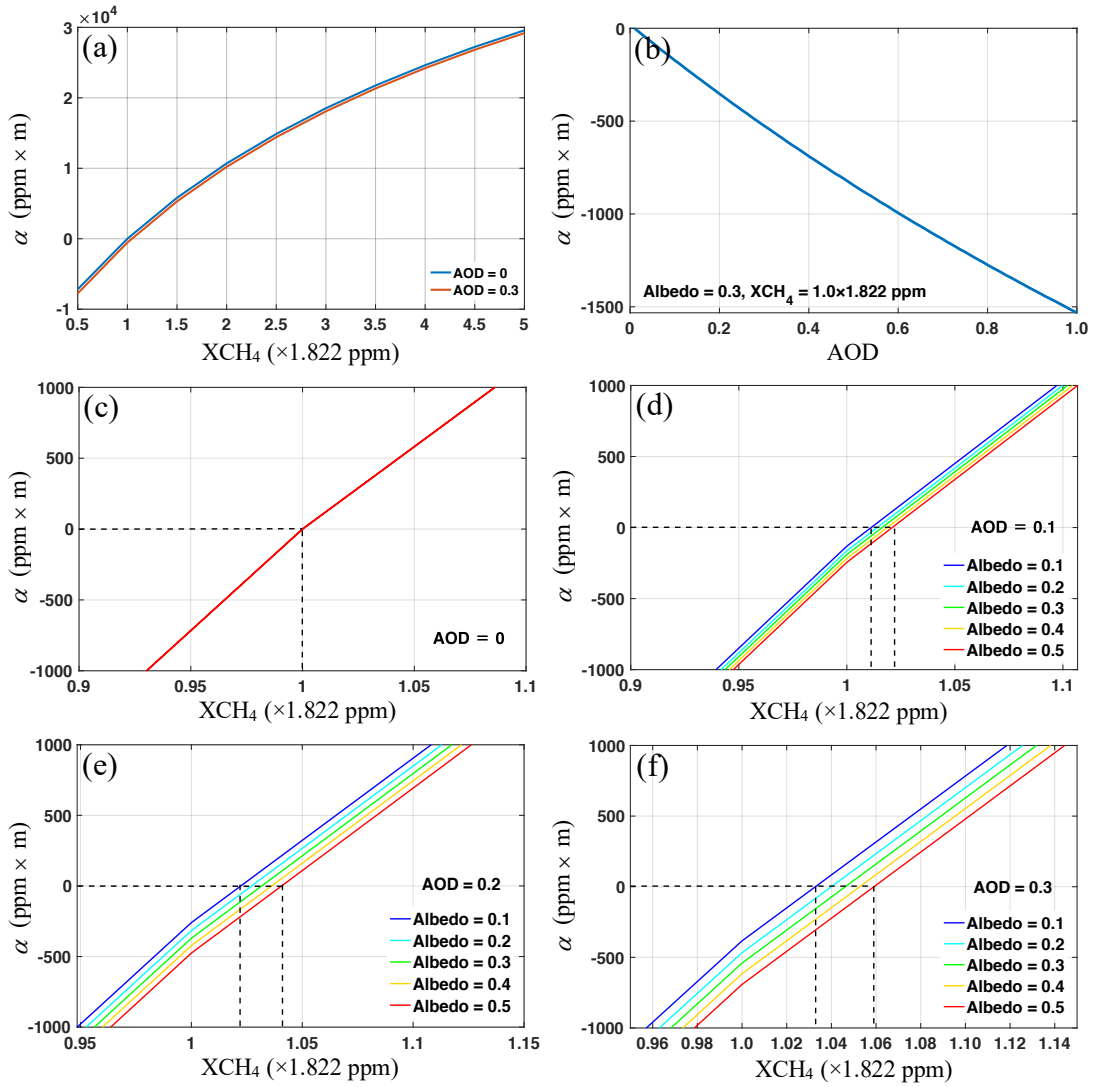

Figure 5: (a) α as a function of XCH_4 for AOD = 0 and AOD = 0.3 (surface albedo = 0.3). (b) α as a function of AOD (XCH_4 = 1.0 × 1.822 ppm, surface albedo = 0.3). Zoomed in versions of α as a function of XCH_4 for different surface albedos (0.1-0.5), where (c) AOD = 0, (d) AOD = 0.1, (e) AOD = 0.2, and (f) AOD = 0.3.

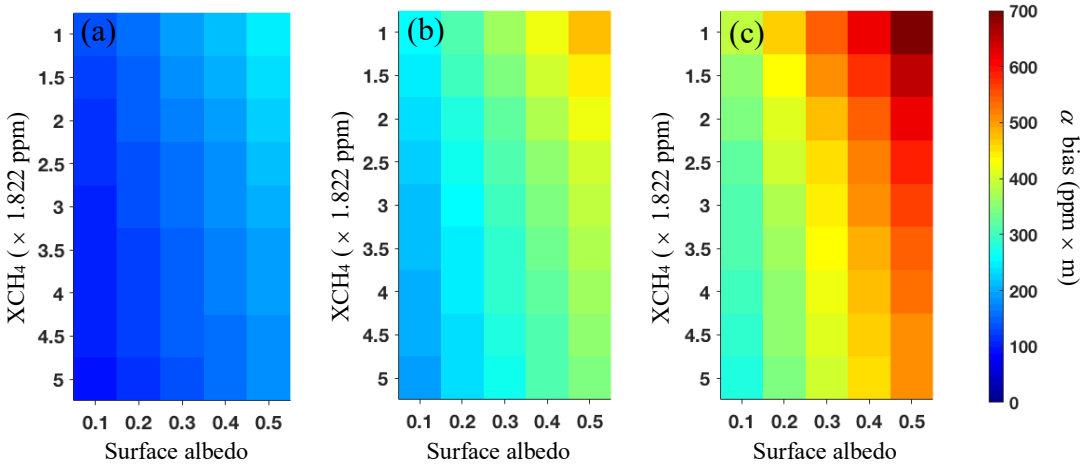

Figure 6: Bias in α as a function of XCH_4 and surface albedo for (a) AOD = 0.1, (b) AOD = 0.2, and (c) AOD = 0.3.

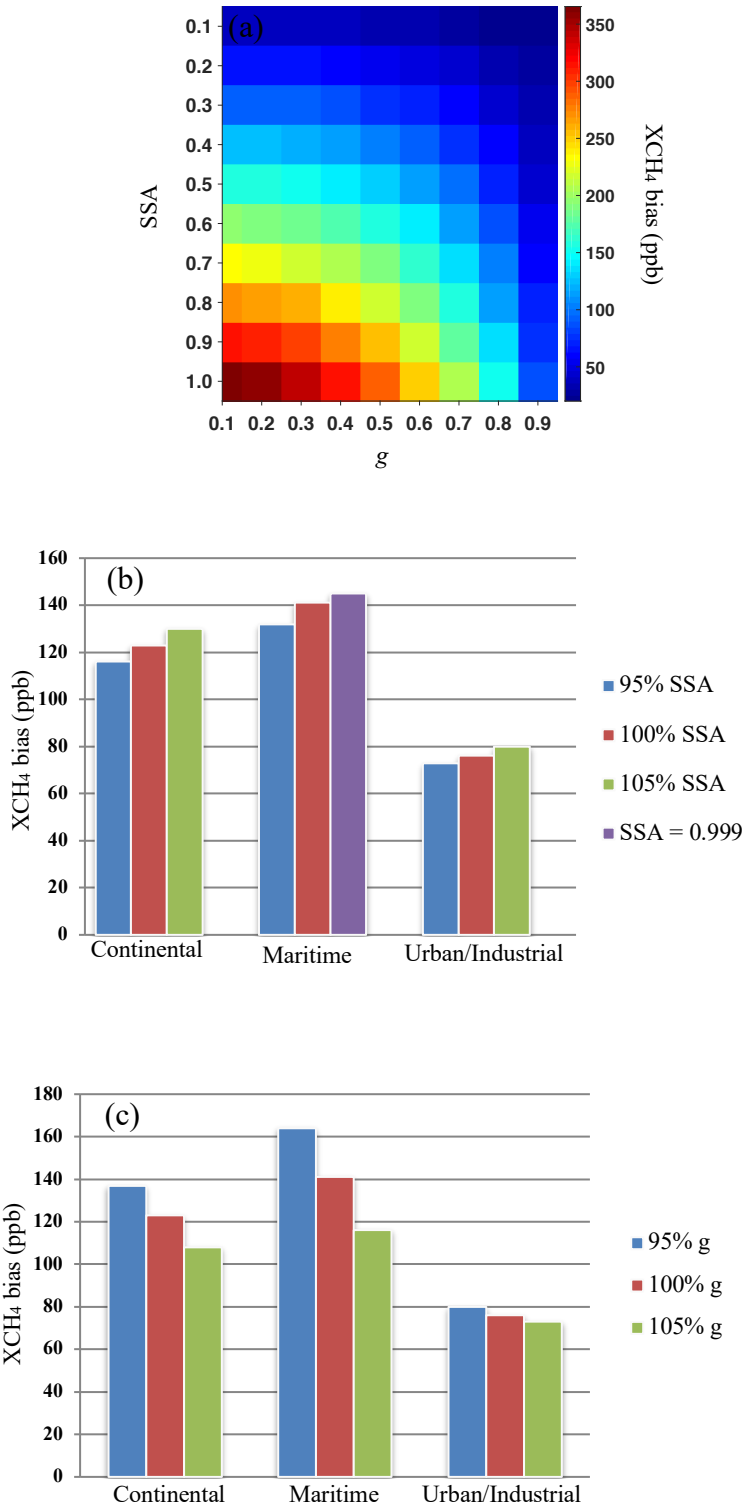

Figure 7: (a) CH_4 retrieval biases for different values of *g* and SSA. Surface albedo, AOD = 0.3, XCH_4 = 1.0 × 1.822 ppm. (b) CH_4 retrieval biases for a ± 5% change in SSA for the three aerosol mixture models. (c) Same as (b), but for a ± 5% change in *g*.

781

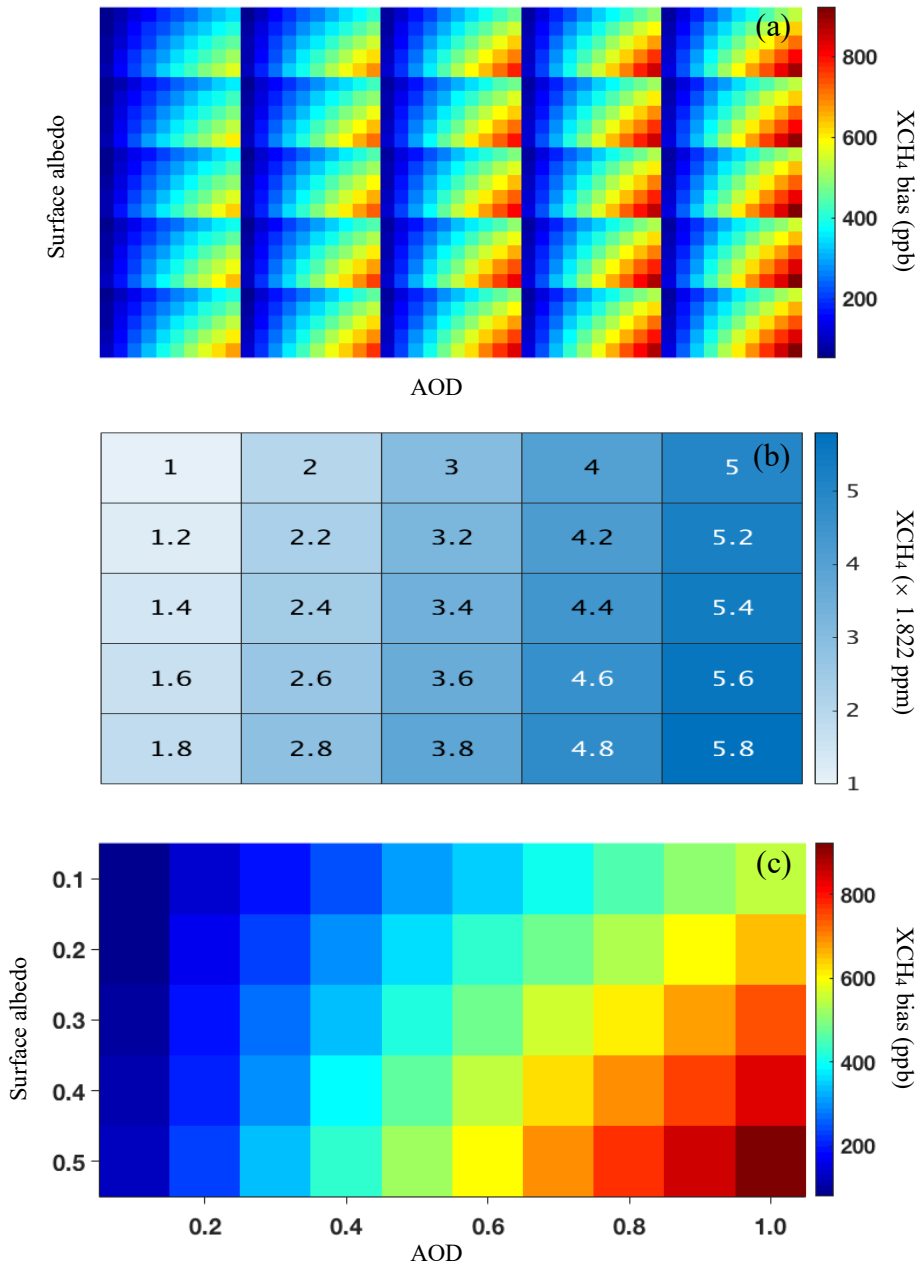
(a)
Surface albedo
AOD
XCH4 bias (ppb)
800
600
400
200
(b)
1 2 3 4 5
1.2 2.2 3.2 4.2 5.2
1.4 2.4 3.4 4.4 5.4
1.6 2.6 3.6 4.6 5.6
1.8 2.8 3.8 4.8 5.8
XCH4 (× 1.822 ppm)
5
4
3
2
1
(c)
Surface albedo
0.1
0.2
0.3
0.4
0.5
0.2
0.4
0.6
0.8
1.0
AOD
XCH4 bias (ppb)
800
600
400
200

782

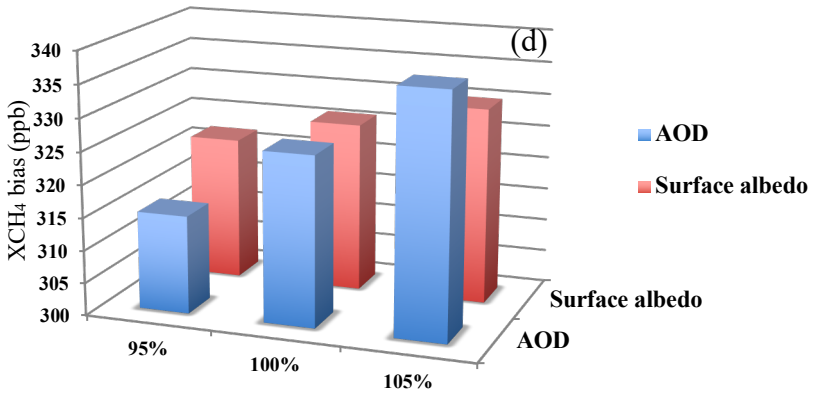

783

784 **Figure 8: (a) CH_4 retrieval biases for different values of XCH_4, AOD and surface albedo. g = 0.75, SSA = 0.95.**

785 **(b) XCH_4 for each box in (a). (c) Zoomed in plot of bottom right box (XCH_4 = 5.8 × 1.822 ppm). The x and y**

786 **axes show the variation of AOD and surface albedo, respectively. These changes are identical for every box**

787 **in (a). (d) CH_4 retrieval biases for a ± 5% change in AOD and surface albedo from a base value of 0.3 (g =**

788 **0.75, SSA = 0.95, XCH_4 = 5.8 × 1.822 ppm).**

789

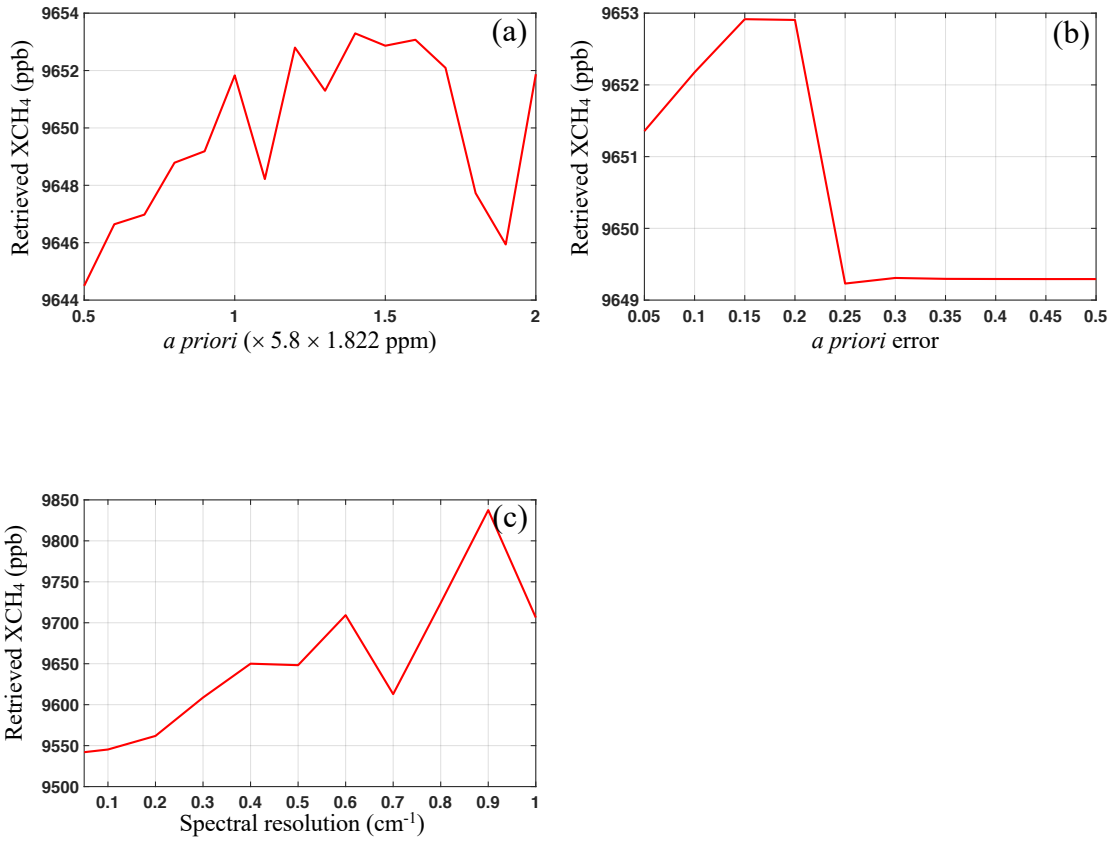

Figure 9: Retrieved XCH_4 for different values of (a) *a priori* (*a priori* error = 0.2), (b) *a priori* error (*a priori* = 5.5 × 1.822 ppm) and (c) spectral resolution. *g* = 0.75, SSA = 0.95, AOD = 1.0, surface albedo = 0.5, XCH_4 = 5.8 × 1.822 ppm.

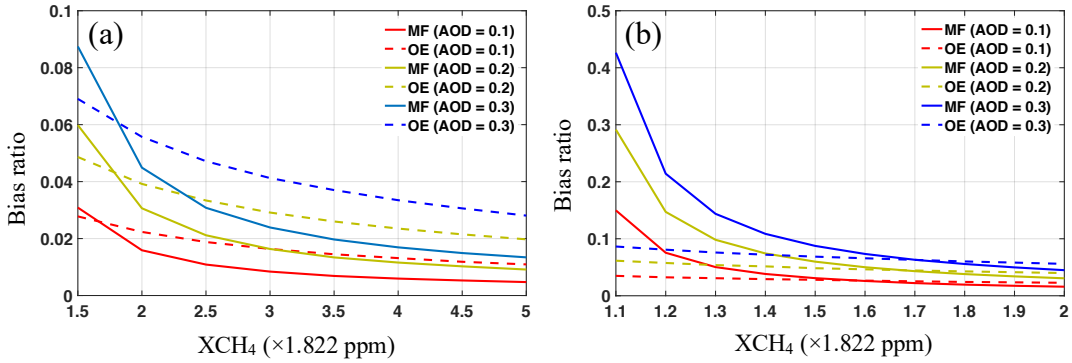

Figure 10: (a) Bias ratio as a function of CH_4 concentration for the two retrieval techniques, where the XCH_4 ranges from 1.5 to 5 (× 1.822 ppm). (b) Same as (a), but for XCH_4 ranging from 1.1 to 2 (× 1.822 ppm). Surface albedo is set to 0.3 for all cases; results for the MF and OE methods are shown by solid and dashed lines, respectively.

804

	Dust-like	Water soluble	Oceanic	Soot
SSA	0.805	0.799	0.970	0.014
g	0.926	0.550	0.816	0.092

805 **Table 1: Optical properties of basic aerosol types (WCRP, 1986).**

806

		Continental	Maritime	Urban/Industrial
Aerosol component	Dust-like	70%		17%
	Water soluble	29%	5%	61%
	Oceanic		95%	
	Soot	1%		22%
SSA		0.746	0.966	0.314
g		0.764	0.810	0.586

807 **Table 2: Optical properties of three aerosol mixture models (WCRP, 1986).**

808

809

Attribute	Values
Sensor height	1 km
View zenith angle	11.91°
Solar zenith angle	30.75°
Relative azimuth angle	22.87°
Aerosol loading region	surface to 1 km
SSA	0.95
g	0.75

810 **Table 3: Inputs for the 2S-ESS model simulation.**

811